Photogrammetric Retrieval of Cloud Advection and Top Height from the Multi-Angle Imaging Spectroradiometer (MISR)

Jia Zong, Roger Davies, Jan-Peter Muller, and David J. Diner

Abstract

This article describes a stereo-photogrammetric method for simultaneous retrieval of cloud advection and cloud-top height fields using multi-angle imagery from the MISR instrument. Although stereoscopy has been widely used for topographic surface retrieval, its application to dynamic cloud elevations has been very limited. This article shows theoretically that, by using multiple MISR camera look angles from satellite altitudes, cloud advection and cloud-top height can be separated stereoscopically, thus enabling their simultaneous retrieval. A completely automatic retrieval algorithm was designed and implemented, including steps for multi-angle image registration on a reference Earth ellipsoid surface, mesoscale cloud advection derivation employing stereoscopic retrieval, and simultaneous stereoscopic reduction of high-resolution cloud-top heights. Before instrument launch, numerical simulations were implemented to demonstrate the feasibility of the retrieval, and to derive estimates of the algorithm errors. Since launch, stereo cloud reduction from MISR has been routinely processed for global climatological studies.

Introduction

The use of photogrammetry for certain types of spaceborne remote sensing data reduction is well established. This includes the examination of images from a single viewing direction, as well as the asynoptic examination of static images from multiple directions. However, the remote sensing of dynamic or ephemeral phenomena from multiple directions constrains the measurements to being nearly simultaneous, and creates new photogrammetric challenges and opportunities.

This situation arose in the development of algorithms to process data from the Multi-angle Imaging SpectroRadiometer (MISR) on the Terra satellite. Here the dynamic targets of interest are clouds, or cloud fields. Their interaction with atmospheric radiation and their feedback effects (which may be positive or negative depending on their type) for future climate change make clouds among the most important components of the Earth's climate system. They are exceedingly heterogeneous, with radiation interactions that are strongly affected by their morphologies. Their reflectivity is decidedly anisotropic, causing difficulties in the use of single angle measurements for the estimation of cloud albedo from space. Consequently, there is considerable motivation to develop remote sensing tools that capture the angular properties of cloud reflectivity while at the same time providing accurate measures of cloud morphology. MISR's pushbroom cameras measure cloud reflectivity from nine different directions over a time period of about 7 minutes, during which time clouds may move. In addition, because cloud-top heights are spatially variable, and the radiometry from different directions must be co-registered to a common surface, a reference altitude must be determined dynamically from the measurements themselves using new stereo-photogrammetric approaches.

Conventional stereo-photogrammetry of static targets requires only two viewing angles. Successful retrievals of cloud-top heights using two simultaneous views from different platforms, or near simultaneous views from the same platform, have been obtained for several case studies (see Hasler (1981) for a review). Kassander and Simms (1957) used stereo observation from both air and ground to determine cloud ranges and cloud-top heights. Roach (1967) analyzed summit areas of severe storms using stereo photos taken from a U-2 aircraft. Hasler (1981) used a stereographic approach to determine cloud heights from simultaneous scans on the GOES East and GOES West satellites with absolute height accuracy of ± 1 to 2 km. Lorenz (1983) described a dedicated polar-orbiting tandem system to eliminate the cloud advection effect while retrieving cloud height. None of these approaches, however, are directly suited to operational retrievals on a global scale from a single orbiter. In addition, the local cloud advection field, as a key constraint obtained separately, also renders an unknown contribution to the retrieval heights. A recent example, ATSR2, has also been shown to allow stereo retrieval of cloud-top height (Lorenz, 1985; Prata and Rurner, 1997), but in this case the maximum resolution is only 1 km and the limited two stereo viewing angles from the conical scan renders it impossible to correct for cloud advection effects without recourse to external data.

The additional angles available with MISR yield an enhanced trinocular stereo approach, which enables simultaneous retrieval of cloud advection and cloud-top height fields on a global basis. These retrievals provide not only a three-dimensional geo-referencing of multi-angle radiances from a

J. Zong and D.J. Diner are with the Jet Propulsion Laboratory, California Institute of Technology, 4800 Oak Grove Drive, Pasadena, CA 91109-8099 (Jia.Zong@jpl.nasa.gov).

R. Davies is with the Institute of Atmospheric Physics, PAS Building #81, University of Arizona, Tucson, AZ 85721.

J.-P. Muller is with the Department of Geomatic Engineering, University College London, Gower Street, London WC1E 6BT, United Kingdom.

Photogrammetric Engineering & Remote Sensing
Vol. 68, No. 8, August 2002, pp. 821–829.

0099-1112/02/6808–821$3.00/0

photogrammetric perspective, but are also of scientific significance in their own right. An initial description of this approach was given in Diner *et al.* (1999b), while this paper addresses the photogrammetric challenges in detail. This paper starts with overviews of the MISR instrument and the cloud-top height data reduction process, followed by a description of the MISR ellipsoid registration process, required as a precursor to stereo cloud retrieval. The next section illustrates the simultaneous retrieval condition and the retrieval algorithm. Experimental results with an error analysis and examples of MISR stereo cloud retrievals are then provided. Conclusions are provided in the last section.

Instrument and Stereo Cloud Reduction Overview

The MISR instrument, a part of NASA's Earth Observing System (EOS), was launched in December 1999 aboard the EOS Terra satellite (Diner *et al.*, 1998). It consists of nine pushbroom cameras, arranged with one pointing toward the nadir (designated An), one bank of four cameras pointing in the forward direction (designated Af, Bf, Cf, and Df in order of increasing off-nadir angles), and another four cameras pointing in the aft direction (using the same convention but designated Aa, Ba, Ca, and Da). Images are acquired with nominal zenith angles with respect to the Earth surface of 0°, 26.1°, 45.6°, 60.0°, and 70.5° for the An, A, B, C, and D cameras, respectively. In order to maximize swath overlap, the MISR cameras also contain small amounts of nominal side looking angles to compensate for Earth rotation (0°, ±1.0°, ±1.7°, ±2.3°, ±2.7° for the An, A, B, C, and D cameras, respectively). Each camera is equipped with four charge-coupled device (CCD) line arrays filtered to provide four spectral bands (centered at 446, 558, 672, and 866 nm). Each line array consists of 1504 photoactive pixels which are digitized with a 14-bit range to prevent the saturation of bright cloud pixels. The cross-track instantaneous field of view and sample spacing is 275m for the off-nadir cameras and 250 m for the nadir camera. The along-track sample spacing is always 275 m; the instantaneous fields of view in this direction depend on camera view angle. The satellite flies in a sun-synchronous descending polar orbit at a 705-km altitude, providing complete global coverage within nine days. Earth imagery is obtained only on the dayside of the orbit. It takes about seven minutes for the MISR instrument to observe any ground region with all nine cameras, providing near-simultaneous multi-angle measurements of the reflected radiance from each region.

The purpose of the MISR instrument is to study the ecology and climate of the Earth through the acquisition of systematic, global multi-angle imagery in reflected sunlight. Routine science data processing of MISR images is conducted at the NASA Langley Distributed Active Archive Center (DAAC). The stereo cloud data reduction is an autonomous and continuous process in order to provide data of scientific value for long-term monitoring and to allow intercomparison with other data sources. Signal data from the MISR are first converted into radiance using radiometric calibration and then are geometrically registered through Level 1 processing. Subsequently, Level 2 science processing extracts geophysical parameters about the Earth's surface, aerosols, and clouds. The main components of the MISR stereo cloud product are the dynamic cloud advection field and a dynamic reference altitude, termed the Reflecting Level Reference Altitude (RLRA). This is defined to be determined by matching features (or areas) with the greatest contrast in the near-nadir viewing directions. Physically, this corresponds to the main reflecting layer, which is typically either the tops of bright clouds, or the terrain surface for clear scenes. The RLRA serves the dual purpose of providing a reference surface for co-registering the multi-angle measurements of cloud reflectivity, needed to calculate cloud albedo, and also as an indicator of cloud altitude, which is helpful for cloud classification. See Diner *et al.* (1999a) and Diner *et al.* (1999b) for details of these applications.

The algorithm for retrieving dynamic cloud advection and cloud-top height is stereophotogrammetric in nature. First, MISR imagery is projected onto a reference Earth ellipsoid surface. Second, the mesoscale cloud advection field (i.e., within grid cells 70.4 km on a side) is determined using trinocular stereo from the ellipsoid-projected MISR imagery with three asymmetrically placed MISR cameras. Finally, the stereo heights, upon which the RLRA is based, containing both clear Earth surface and cloud-top heights, are determined from image matching of near-nadir MISR imagery at a 275-m resolution and are reported at a 1.1-km resolution.

Image Registration and Simulation Results

The MISR instrument images instantaneously specific locations within a segment of 2800 km on the Earth's surface in the along-track direction, as shown schematically in Figure 1a. All 36 channels of imagery (from nine cameras and four bands, shown as stacked boxes) need to be projected onto the same Earth reference ellipsoidal surface, for several reasons. First, stereo cloud retrievals need to be derived at known geographical locations. Second, stereo image matching is more efficient from images rectified to epipolar or near-epipolar geometry. Third, construction of the RLRA on a global basis from stereo disparities is favored by a smooth and analytical base surface, i.e., stereo heights are calculated relative to the zero-elevation reference ellipsoid surface. The Space-Oblique Mercator (SOM) map projection (Snyder, 1987) is used for the georegistration. In Figure 1b, the radiometrically corrected and georectified radiance products from Level 1 processing represent a continuously superimposed set of multi-angle, multi-spectral data. In an abstract world, these may be looked upon as the data collected by a "virtual" MISR. Theoretically, ground features at zero elevation relative to the surface ellipsoid have no image disparities, whereas in reality, image disparities of zero-elevation features would indicate the present of misregistration errors.

Ellipsoid Surface Registration

The ellipsoid projection is required to be both accurate and automated. Ignoring dynamic errors in the navigation data, the algorithm relies on a transform which efficiently maps the local

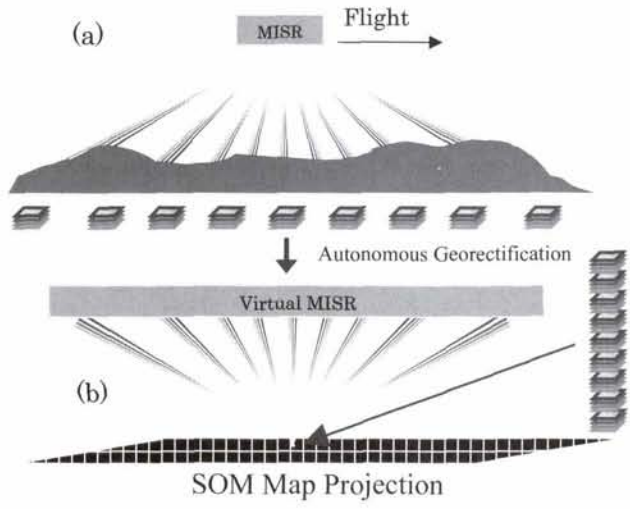

Figure 1. (a) MISR physical imaging event. (b) Georectified radiance product.

ellipsoid surface represented in the SOM space directly to MISR image space based on four simple geometric elements: linear camera geometry, near circular orbit, smooth Earth rotation, and ellipsoid curvature. A pair of ellipsoid transforms can be represented in polynomial form as follows:

$$l_{img} = c_1 + c_2\Delta l_{som} + c_3\Delta s_{som} + c_4\Delta s_{som}^2 + c_5\Delta l\Delta s + c_6\Delta s_{som}^3 \quad (1)$$

$$s_{img} = d_1 + d_2\Delta l_{som} + d_3\Delta s_{som} + d_4\Delta s_{som}^2 + d_5\Delta l\Delta s + d_6\Delta s_{som}^3 \quad (2)$$

where l_{img} and s_{img} are image line and sample coordinates, $\Delta l_{som} = l_{som} - (l_{som})_0$ and $\Delta s_{som} = s_{som} - (s_{som})_0$ are SOM grid indices relative to a center location assuming no distortion over SOM space, and c_i and d_i $(i = 1, \ldots, 6)$ are the ellipsoid transform coefficients. One ellipsoid transform is independently derived and applied to each of the 36 channels of MISR imagery using tie-points that are evenly spaced throughout the SOM segment which the transform covers. The image coordinates of the tie-points are determined using backward intersection. The underlying principle of backward projection is the collinearity equation which converts look vectors from ground space to image space according to orbit navigation and camera geometry, as described in Jovanovic *et al.* (1996). The ellipsoid transform coefficients are solved for by a least-squares fit of the tie-points. Once built, an ellipsoid transform is applied to resample the radiance value from MISR imagery to the ellipsoid surface at every 275-m location on the SOM map grid.

Prelaunch Simulation and Results

For prelaunch testing, MISR imagery was first simulated based on georegistered Landsat Thematic Mapper (TM) data along with a registered digital elevation model (DEM). The simulation process made use of simulated nominal orbit navigation data and a camera geometric model. The details are described in Lewicki *et al.* (1994). A set of "truth" or "expected" data was also created by intensively backward projecting from the surface ellipsoid up to MISR imagery at each predefined 275-m resolution SOM grid point, resulting in the "expected" mapping of the MISR image coordinate at the grid. For this particular test, a segment of test data and expected data was created for a North American region between latitude 20° and 30° north and longitude 100° and 120° west.

The ellipsoid projection was tested using simulated nominal navigation data with added measurement errors. The georegistration accuracy was expected to be partially dependent on errors in the navigation data, and partially on the ellipsoid transform. Comparing the ellipsoid projection with the "expected" data, it was found that, at the 95 percent confidence level, the errors in the ellipsoid projection were generally less than 0.6 pixels in the along-track direction and 0.3 pixels in the cross-track direction using the worst case predicted orbit performance. These accuracy estimates vary slightly from one camera to another, with oblique cameras usually containing larger errors. To estimate errors arising purely from the algorithm design, the same test was also run using simulated nominal navigation data without measurement errors. In this case, at the 95 percent confidence level, the along-track error was less than 0.3 pixels and the cross-track error was less than 0.2 pixels.

Epipolar Nature of Ellipsoid-Projected Imagery

In photogrammetry, a pair of stereo images are in epipolar geometry when they are leveled at the same elevation and rotated such that conjugate image features along the epipolar direction in one image can always be found along the same epipolar line in the other image. In other words, image disparities caused by objects with different heights lie in one dimension, the so-called epipolar direction. This dramatically improves image matching efficiency because the search space for matching is reduced from two dimensions into one dimension. Theoretically, a true epipolar condition exists only for central-perspective images (Kim, 2000). However, rectifying linear-perspective MISR imagery to the zero elevation ellipsoid surface creates a confined similarity, that is, local epipolarity exists where the Earth curvature effect can be ignored.

To demonstrate the epipolarity of the ellipsoid projection, let A and B be a pair of MISR cameras. In Figure 2, a is a look vector for MISR camera A, and b is the conjugate look vector from camera B. Look rays a and b intersect at a presumed cloud location C, then intersect with the surface ellipsoid at P and Q, respectively. Now we assume there is a lower cloud C' which intersects the same look vector a from camera A and another look vector b' from camera B. Because look vectors of the same camera do not vary much locally, look vector b' is then nearly parallel to look vector b and its intersection with the surface ellipsoid at Q' must lie on line PQ. Obviously, direction PQ defines the local epipolar line for the stereo camera pair A and B.

Numerical Simulation and Results

To verify the epipolarity of the ellipsoid projection, sparse cloud features were randomly "planted" over a simulated swath in SOM space, then backward-projected up to MISR image space, and then forward-projected down to the ellipsoid surface along the look vectors of the two stereo cameras. Disparities were measured in degrees relative to the along-track direction in SOM space. Figure 3 shows the epipolar directions of the An camera relative to the forward camera set versus the cross-track pixel sample. Note that the illustrated swath is wider than a standard MISR swath of 1504 pixels to account for cross-track swath shift of all nine cameras. These examples indicate that the epipolar direction forms a small angle relative to the swath along-track direction. This small angle varies slightly across the MISR swath. For the convenience of implementation, one local epipolar direction was determined within each $(70.4 \text{ km})^2$ domain. To show this is sufficient, the disparity at every 8.8-km posting within each $(70.4 \text{ km})^2$ domain was tested. The elevations of the sample cloud features ranged from 5 km to 20 km above the surface ellipsoid. The results indicated large disparities along the local epipolar direction, depending directly on the height of the sample cloud feature. For example, for clouds at 10 km and 20 km above the surface ellipsoid, their image disparities in the epipolar direction for the An-Af camera pair are 18.2 pixels and 36.5 pixels, respectively. The deviations of disparities from the cross-epipolar direction within the domain were trivial: less than 0.1 pixels in all test cases. The

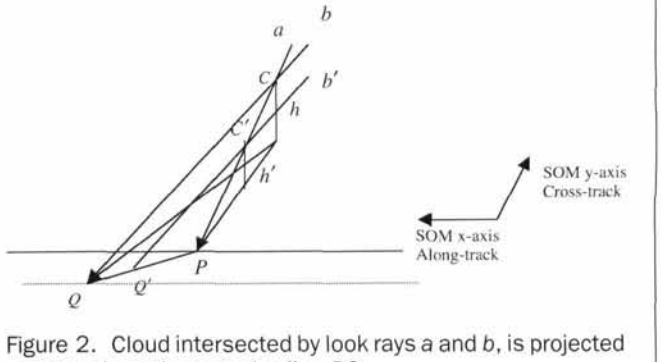

Figure 2. Cloud intersected by look rays a and b, is projected on SOM along the epipolar line PQ.

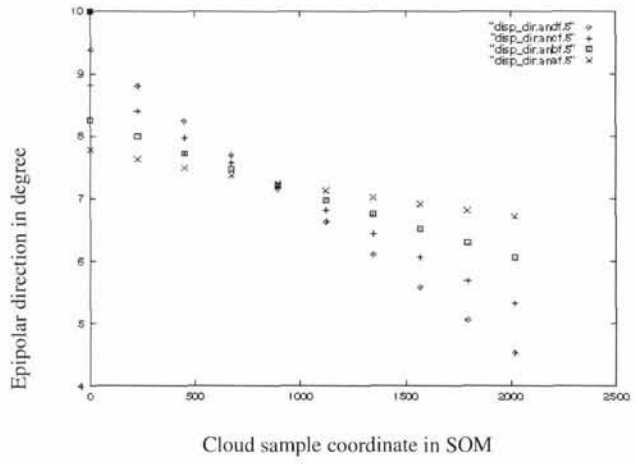

Figure 3. Epipolar directions of camera An to camera Af, Bf, Cf, and Df.

same test was repeated at latitudes 20° and 55°. The epipolar directions vary slightly but the epipolar conditions behave the same. Therefore, for stereo cloud retrieval, the image matching search window on ellipsoid-projected imagery needs only to be on a long rectangle aligned with the local epipolar direction, and the extension to the cross-epipolar direction needs only to account for cloud advection.

Stereo Retrieval Algorithm

The key to stereoscopic retrieval of an object surface is to determine heights from image disparities. In MISR's case, a static cloud or terrain feature above the Earth ellipsoid surface causes an image disparity as shown in Figure 4 as $\overline{AB_1}$ where A and B_1 are the conjugate image features of the object projected onto the ellipsoid surface. The object height h relative to the Earth reference ellipsoid is the intersection of conjugate look rays $\bar{a}$ and $\bar{b}_1$. In the case of a dynamic cloud feature with a velocity component in the flight direction, the disparity $\overline{AB_2}$ is caused by the combined effect from both the cloud-top height and the advection. Direct intersection of look rays $\bar{a}$ and $\bar{b}_2$ would result in an incorrect height h', compared to the true height, h. Figure 4 illustrates a major barrier presented in the stereoscopic retrieval of cloud-top height, that is, both cloud advection and top height contribute to image disparities and, with two cameras, these are not separable. In order to obtain accurate cloud-top height globally, given conditions of substantial cloud advection, it is necessary to separate the disparities due to cloud advection from those due to height.

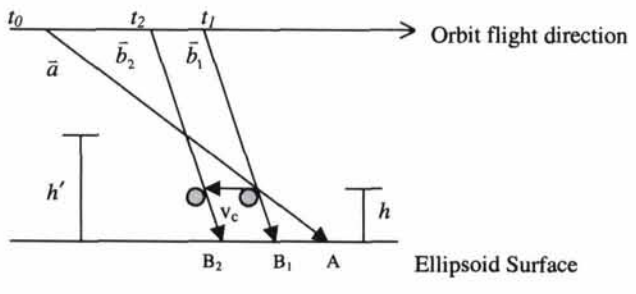

Figure 4. Disparity of a cloud in two images observed with different view angles.

Stereo Retrieval Condition

Figure 5 is used to illustrate the stereoscopic separation condition. It shows the geometry of MISR imaging in the along-track direction. The shaded circles are cloud locations at times t_i with i denoting camera indices, assuming a constant along-track cloud advection v_c. The projections of the cloud onto a reference ellipsoid surface are at the locations x_i at these times, with the discrete MISR camera view angles θ_i. For simplicity in this discussion, the Earth's surface is assumed to be spherical and the cloud advection and the camera look vectors are assumed to lie in the along-track plane. Assuming a cloud edge is seen by two cameras with different view angles at times t_1 and t_2, respectively, the following equations represent the distances traveled by the spacecraft and that of the cloud during this time interval:

$$v_s(t_2 - t_1) = (R + H)(\alpha_2 - \alpha_1) - (R + H)(\Gamma_2 - \Gamma_1) \quad (3)$$

$$v_c(t_2 - t_1) = (R + h)(\alpha_2 - \alpha_1) - (R + h)(\gamma_2 - \gamma_1) \quad (4)$$

where v_s is the spacecraft velocity in the along-track direction, R is the radius of the Earth, H is the orbit altitude, and h is the cloud-top height. In Figure 5, α_1 and α_2 are the angles between an initial radial line at time t_0 and the radial line passing the image locations x_1 and x_2, respectively; Γ_1 and Γ_2 are the angles between the radial lines to the spacecraft and the corresponding image locations x_1 and x_2; and γ_1 and γ_2 are the angles between the radial lines to the cloud and the corresponding image locations x_1 and x_2. Because h is much smaller than R, Equation 4 can be rewritten as

$$v_c\,(t_2 - t_1) = (x_2 - x_1) + h(\tan\,\theta_1 - \tan\,\theta_2). \quad (5)$$

With multi-angle images, Equation 5 can be generalized into a linear system as follows:

$$v_c\,(t_j - t_i) - h(\tan\,\theta_i - \tan\,\theta_j) = (x_j - x_i)$$
$$(i, j) = 1, 2, \ldots, n,\ i \neq j,\ n \geq 3 \quad (6)$$

The linear system expressed by Equation 6 represents a straight line in the $\Delta x = (x_j - x_i)$ versus $\Delta t = (t_j - t_i)$ space. Matching at least three images with different view angles θ_i is required to solve for v_c and h from this linear system. However,

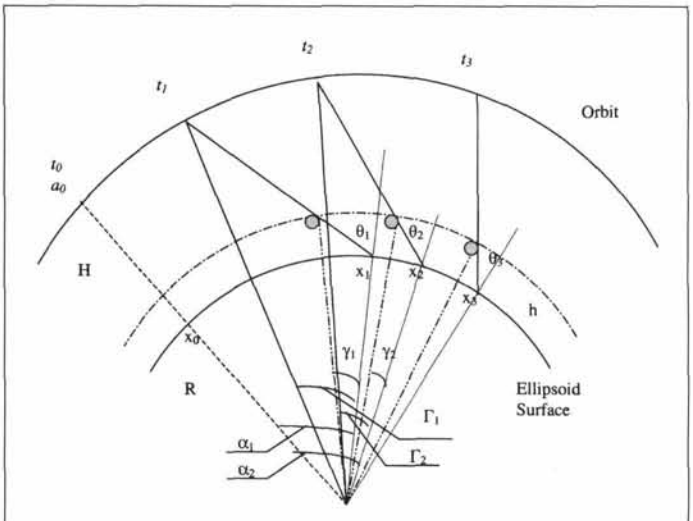

Figure 5. Geometry of a cloud observed by three MISR cameras with different view angles in the along-track direction.

any two linear equations are dependent on each other if their determinant is zero: i.e.,

$$\det A = (t_i - t_{i-1})(\tan\theta_i - \tan\theta_{i+1}) - (t_{i+1} - t_i)(\tan\theta_{i-1} - \tan\theta_i) = 0. \quad (7)$$

In such a case, v_c and h are inseparable. On a scale where the flight line is straight and the surface is a plane (e.g., from an aircraft), this singularity will always be true. From orbital altitude over a spheroidal or an ellipsoidal surface, however, the time interval traveled between a pair of cameras does not linearly relate to the tangent of view angles as depicted in both Figure 5 and Equation 3, as long as the selected camera view angles do not happen to be symmetric around the nadir view. This condition therefore breaks the singularity and allows us to independently solve the linear system represented by Equation 6 for v_c and h.

Camera Triplet for Simultaneous Retrieval

Although the illustration above is one-dimensional, the same argument holds true for the cross-track direction where the stereo effect is much smaller due to smaller camera side-look angle differences. Ideally, a longer time span between camera views provides higher accuracy in cloud advection retrieval. Naturally, selection of either the forward or the aft An, B, and D camera triplet provides not only the best separation condition, but also the highest accuracy in cloud advection retrieval. The reliability of the retrieval is optimized by performing a retrieval using a forward-viewing set of cameras and checking the result against a retrieval using an aft-viewing set. In case a default camera triplet can not be formed due to missing data in any candidate camera, a neighboring camera can be substituted. However, new camera triplets must satisfy the condition that the determinant, detA, remains large enough to avoid any singularity. A threshold is established through the simulation test, as will be discussed later.

Cloud Advection Field Retrieval

The cloud advection field is derived from three asymmetric MISR cameras according to the simultaneous retrieval principle. In practice, cloud fields may move three-dimensionally and multi-layer clouds may move differently. In MISR's case, the stereo retrieval of cloud field is limited by the following assumptions: (1) the cloud advection velocity is uniform over a mesoscale domain (70.4 km)^2, (2) vertical cloud advection is ignored during the 7-minute time interval between camera Df and Da views because vertical cloud motion is likely to be small for all clouds except strongly convective ones, and (3) no more than two cloud layers are present. In addition, due to the heavy computational load of global processing, the retrieval algorithm needs to be balanced between accuracy and efficiency.

Stereo Image Matching

A combination of feature-based and area-based matching schemes was developed. First, hierarchical sets of local maximum radiances are independently detected from both target and matching imagery. Each set in the hierarchy is a subset of the previous set, ending with the brightest radiance in each image. Features in the target sets are then matched with features of the candidate sets in a search window. The search window is on the surface ellipsoid in SOM space, oriented along the epipolar direction with a length that accommodates the highest allowed cloud-top height and expanded to include cloud advection. This feature-based matcher, named Nested Max (NM), is applied to quickly match a sparse subset of bright conjugate features with high confidence. It is then followed by a fast area-based matcher, called the multipoint matcher (M2), which uses a metric computed by taking all image values within a patch, subtracting the mean value within the patch from each pixel, and then normalizing by the difference between the maximum and minimum values. The difference of this metric from the target and matching patch is then averaged over the patch area and normalized by an uncertainty estimate, and finally tested against a threshold. M2 is used to select the best matches among the list of candidates created by NM.

3D Ray Intersection

Assuming that there is no vertical cloud motion but a constant horizontal cloud advection, the cloud advection vector, the conjugate look rays from image matching of D, B, and An cameras, and the surface disparities should form a closed loop in a three-dimensional Cartesian coordinate as shown in Figure 6 and represented by the following equations:

$$\overrightarrow{P_1P_2} = \lambda_2\hat{b} + \vec{v}_c(t_2 - t_1) - \lambda_1\hat{a} \quad (8)$$

$$\overrightarrow{P_2P_3} = \lambda_3\hat{c} + \vec{v}_c(t_3 - t_2) - \lambda_2\hat{b} \quad (9)$$

where P_1, P_2, and P_3 are the conjugate image locations of the same cloud edge projected on the ellipsoid surface; $\hat{a}$, $\hat{b}$, and $\hat{c}$ are the known unit vectors of the conjugate look rays; $\vec{v}$ is the unknown cloud advection velocity; and λ_1, λ_2, and λ_3 are the unknown scale factors of the look rays for them to intersect with the cloud, respectively. We now represent this relationship in a local coordinate system such that its z-axis is aligned with the zenith direction at nadir image point P_3. The x-axis and the y-axis are aligned with the north and east directions, respectively. The condition of no vertical cloud motion $v_{cz} = 0$ is imposed. The remaining unknowns, the horizontal cloud advection (v_{cx}, v_{cy}) and the ray scale factors (λ_1, λ_2, λ_3) are solved for simultaneously with the above six equations. The cloud-top height, h, of this matched triplet is obtained by projecting the nadir view look ray, e.g., $\lambda_3\hat{c}$, onto the normal direction at the ellipsoid surface as $h = \lambda_3\hat{c} \cdot \hat{n}$.

Mesoscale Cloud Advection

Based on the assumptions that local cloud advection vectors at each (70.4 km)^2 domain are constant, the velocities of the cloud spots derived from image matching and ray intersection within a domain are sorted in a two-dimensional histogram, where each bin of the histogram corresponds to the north-south and east-west advection speed with a bin width of 6 m/s. Next, the mean motions and median heights of the two most popular bins are computed, which helps to assign one of these two bins to be the low-cloud bin, and the other one to be the high-cloud bin.

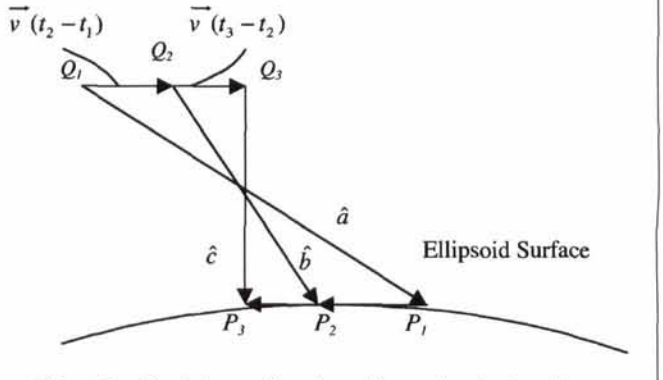

Figure 6. Ray intersection to retrieve cloud advection.

An added benefit of histogram binning is that the process removes potential blunders from matching and improves the retrieval reliability. The low- and high-cloud bins potentially correspond to either the ground surface and one cloud layer, or one low-cloud layer and one high-cloud layer which may advect in different directions.

Cloud-Top Height Retrieval

Once local cloud advection vectors are derived, they provide corrections to the conversion of high-resolution image disparities to heights. The high-resolution image disparity field on a 1.1-km grid is derived with a combination of area-based matchers: M2 and the multipoint matcher with medians (M3). M3 is a slight variation of M2 with higher coverage but lower computational speed. Therefore, M2 is applied first, followed by M3 (Diner *et al.*, 1999b). Errors are reduced by requiring similar results from two pairs of near-nadir cameras, nominally Af-An and Aa-An.

Depending on the mesoscale cloud advection, two search windows may be defined for both high-cloud and low-cloud bins. These search windows are aligned with the epipolar direction to accommodate the altitude range of the two cloud bins.

The cloud-top height is constructed by a three-dimensional ray intersection, with an allowable minimum distance $\hat{d}$ between the conjugate rays $\hat{a}$ and $\hat{b}$ as $\hat{d} = \hat{a} \times \hat{b}$. In the static case as shown in Figure 7a, where $\vec{p}$ denotes the vector connecting the conjugate points P_1 and P_2 from image matching and $\lambda_1, \lambda_2, \lambda_3$ are the scale factors to the corresponding look vectors, ray intersection requires that the four vectors $\vec{p}$, $\lambda_2\hat{b}$, $\lambda_1\hat{a}$, and $\lambda_0\hat{d}$ close to a loop. In Figure 7b, where a dynamic cloud moves with a velocity $\vec{v}_c$ during the time interval Δt between the conjugate cloud features seen by the cameras involved, cloud advection vector $\vec{v}_c\Delta t$ must be taken into the loop for correct ray intersection as

$$\vec{p} - \vec{v}_c\Delta t = \lambda_2\hat{b} + \lambda_0\hat{d} - \lambda_1\hat{a}. \tag{11}$$

Vector Equation 11 contains three equations and three unknowns $\lambda_0, \lambda_1, \lambda_2$ for each matching pair. The cloud-top location is obtained starting from the nadir image location P_2: i.e.,

$$C = P_2 - \lambda_2\hat{b} - \frac{1}{2}\lambda_0\hat{d}. \tag{12}$$

For each matching point pair, if the image disparity is associated with the image matching search window of one cloud bin only, the cloud advection vector of that cloud bin is used in Equation 11. Otherwise, if the image disparity is in the union of two search windows, the average cloud advection vector of the two cloud bins is used instead, although the confidence of the retrieval in such a case is lower due to a larger uncertainty in the cloud advection correction. Finally, the cloud-top height is established based on both Af-An and Aa-An results, with an identifier to indicate the retrieval confidence based on various factors: the uncertainty of cloud advection vector (single or union), the source matcher (M2 or M3), the minimum distance between the intersecting look rays, and the difference between the forward and aftward results.

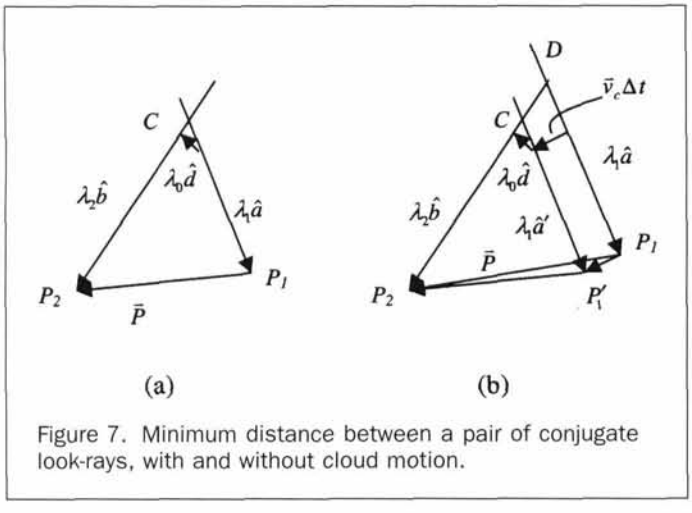

Figure 7. Minimum distance between a pair of conjugate look-rays, with and without cloud motion.

TABLE 1. CLOUD ADVECTION RETRIEVAL TEST RESULTS

Cam. Triplet	Deta$A$ (line)	Δv_{cx} (m/s)		Δv_{cy} (m/s)		Δh (m)	
		$\sigma_{v_{cx}}$	Max	$\sigma_{v_{cy}}$	*Max*	σ_h	*Max*
An-Bf-Df	−1230	0.35	0.89	0.03	0.08	22.1	53.5
Aa-Bf-Df	−1892	0.36	0.88	0.03	0.09	26.0	60.8
An-Bf-Aa	−41	0.92	2.96	0.15	0.49	84.5	268.0
An-Bf-Ba	−6	12.2	36.5	1.72	5.08	1103	3284

Experiments and Results

Separability and Error Analysis

Pre-launch simulation tests were created to illustrate the feasibility and the error analysis of the simultaneous retrieval methodology.

Separability and Theoretical Accuracy

To demonstrate the separability of cloud advection and cloud-top height with MISR data and to calculate the theoretical accuracy of the retrieval, we again simulated cloud features across the MISR swath. Around 100 independent "cloud spots" were planted in space with known heights (within a range of 1 to 20 km above zero elevation) and advection vectors (in various horizontal directions and values of 0, 12, 24, and 48 m/s). Table 1 summarizes the retrieval results. Column one lists the MISR camera triplet used for simultaneous retrieval. Column two contains the nominal determinants of each camera triplet according to Equation 7. The remaining columns list the errors in cloud advection and height retrieval Δv_{cx}, Δv_{cy}, and Δh, with x indicating the along-track direction and y the cross-track direction. σ is the standard deviation of the retrieval error comparing with the true cloud seeds. *Max* is the maximum error observed. For asymmetric camera combinations An-Bf- Df and Aa-Bf-Df, the maximum cloud advection deviation is less than 1 m/s from the true value and maximum cloud-top height deviation is less than 60 m. On the other hand, for near symmetric and symmetric camera triplets An-Bf-Aa and An-Bf-Ba, their determinants are too close to zero to provide reliable retrievals.

Error Analysis

Whereas the simulation results demonstrate the feasibility of simultaneous retrieval, the actual retrieval accuracy is affected by practical limitations, namely, the multi-angle co- registration accuracy, the image matching accuracy, and the sensitivity of the simultaneous retrieval model to input measurements, i.e., image disparities.

Simulation testing has previously predicted that ellipsoid co-registration error will be less than 0.6 pixels in the along-track direction and 0.3 pixels in the cross-track direction. The area-based matcher M2 used for stereo retrieval has also been verified to be accurate to the pixel level (Diner *et al.*, 1999b), i.e., $\sigma_{match} \approx 0.5$ pixels. The combined accuracy in image disparity is then less than a pixel: i.e.,

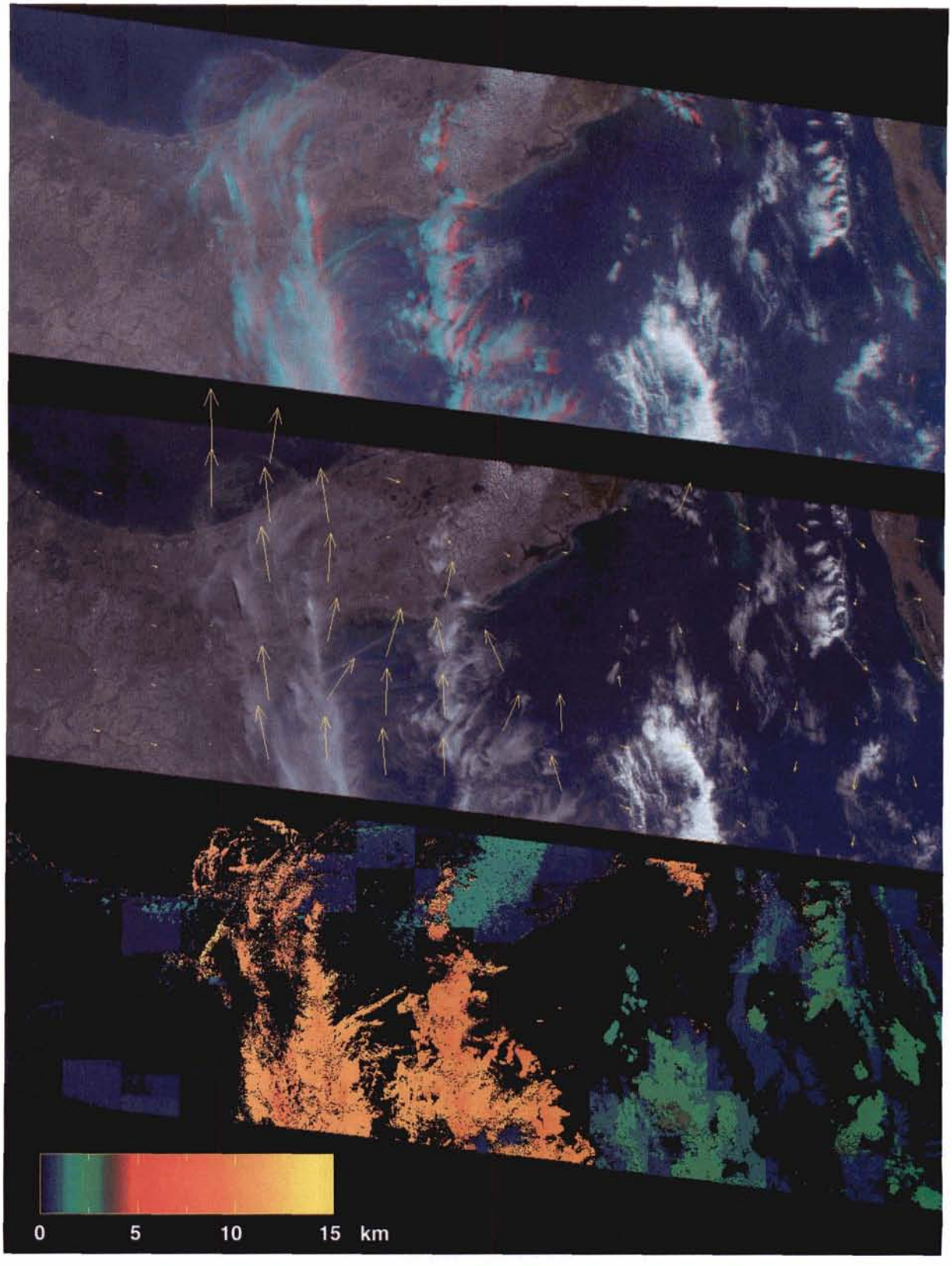

Plate 1. Top: MISR stereo anaglyph over Florida and Cuba from orbit 1155, 06 March 2000. North is at the left. Middle: Stereo retrieved cloud advection field. Arrow length is proportional to velocity. The maximum vector length corresponds to about 40 m/s. Bottom: Stereo height field.

TABLE 2. SENSITIVITY OF SIMULTANEOUS RETRIEVAL

Cam. Triplet	Added Input Errors in Image Disparity	σ_h (m)	σ_{v_a} (m/s)	σ_{v_c} (m/s)
Df-Bf-An	σ_l = 275 m in An or Df	600	10	2
	σ_l = 275 m in Bf	1200	17	3
Df-Bf-Aa	σ_l = 275 m in An or Df	500	6	1
	σ_l = 275 m in Bf	1000	13	3

$$\sigma = \sqrt{\sigma_{geo}^2 + \sigma_{match}^2} = \sqrt{0.6^2 + 0.5^2} \approx 0.8. \quad (13)$$

The simultaneous retrieval model (Equations 8 and 9) can be represented as a linear system $y = \mathbf{A}x$, where y is the measurements of image disparity, $\mathbf{A}$ is the design matrix depending on the geometry of camera triplet, and x is the unknown cloud advection vector and top height. The covariance of the estimated unknowns $\boldsymbol{Q}_{xx} = \sigma_y(\mathbf{A}^T\mathbf{A})^{-1}$ depends both on the input error σ_y and the geometry of camera triplet. Table 2 shows a couple of examples of error propagation to cloud advection in the along-track direction σ_{v_a} and cross- track direction σ_{v_c} and cloud-top height error σ_h for camera triplets Df-Bf-An and Df-Bf-Aa, by introducing one-pixel line errors (275 m) in the simulation process (error propagation in the sample direction is trivial). In summary, the lessons are (1) simultaneous stereo retrieval is sensitive to errors present in the input image disparity. In particular, errors in the middle camera of a triplet cause the greatest instability. To avoid it, image matching always uses imagery from the middle camera as the target to match to the other two (i.e., Bf-Df and Bf-An). (2) Camera triplet Df-Bf-Aa, with a higher determinant value according to Table 1, actually performs more reliably than the natural choice Df-Bf-An. Due to existing constraints in the current software, the nadir camera (An) remains in the default triplet but Df-Bf-Aa may be considered for future implementations. For alternative camera triplets, the determinant threshold must be high enough (i.e., 1000 lines) to enable sensitive retrievals. (3) Table 2 shows large errors are associated with a biased individual retrieval. However, the average advection field is derived statistically from the velocity histogram. As long as there are enough inputs with no systematic bias, the retrieval can be accurate up to 3 m/s according to an error analysis with numerically simulated cloud fields using simplified geometry (Horvath and Davies, 2000).

Finally, the accuracy of stereoscopically retrieved cloud-top height surface depends on the accuracies of both stereo image matching and cloud advection retrieval. With simulation of cloud at various advection speeds and heights, the results indicate that a one-pixel line error (275 m) in image disparity results in about a 300-m error in cloud-top height retrieval, and 3 m/s errors in cloud advection in the along-track direction or cross-track direction result in up to 300 m or 100 m errors in the height retrieval, respectively.

Stereo Retrieval Example

The MISR instrument cover was opened in February 2000. To estimate the accuracy of simultaneous stereoscopic retrieval, clear surface scenes were first tested, because retrieval velocities are expected to be zero and heights should match the terrain surface. Next, retrieved cloud-top heights and advection vectors were used as cloud seeds, backward projected up to MISR image space, and visually examined to ensure correspondence with the correct conjugate cloud features. Additional, intensive validation of MISR stereo product accuracies has been conducted with case studies using independently derived cloud advection velocities and cloud-top heights from GOES (Horváth and Davies, 2001). In brief, these tests confirmed that the accuracy for the retrieved mesoscale cloud field velocity is around 3 m/s, matching the expectation of pre-launch error analysis. Stereoscopically retrieved cloud-top height is expected to be accurate up to 300 to 800 m nominally, with the surface and low clouds likely to be more accurate than the high cloud. At boundaries between high-cloud and low-cloud layers, the stereo height could be less accurate, with error up to 1 to 2 km. As an example, Plate 1 shows an early segment of MISR ellipsoid-projected imagery over Florida and Cuba from Terra orbit 1155. The top panel is an anaglyph constructed from cameras Aa and Ca. The stereoscopic effect can be observed by using a pair of red/blue anaglyph glasses (red filter over left eye). The imagery has been oriented with north at the left to facilitate stereo viewing. Measurements along the coastlines (at zero elevation) of ellipsoid-projected imagery indicated georegistration and coregistration met the pre-launch expectation. The middle panel is an Aa image with vectors indicating the stereo retrieved cloud advection field. The bottom is the stereo height retrieval, with high cloud detected in the central area, and low cloud over the land and the right side of the imagery. Some blockness in the height retrieval is noted, which is related to the accuracy of the simultaneously retrieved cloud advection field from discrete local domains (each 70.4 km on one side). Compared with the knowledge of surface elevation, we found the maximum surface deviation is less then 350 m for the worst domain. More systematic validation of MISR stereo cloud advection retrievals can be found in Horváth and Davies (2001).

Summary and Conclusion

In this paper, a photogrammetric approach to simultaneous stereoscopic retrieval of cloud advection and cloud-top height from space is demonstrated to be practicable. An automatic algorithm has been designed and implemented for global retrievals. It is currently producing operational global cloud-top products. Numerical simulations indicate a theoretical accuracy of better than 1 m/s for cloud advection and around 60 m for cloud-top height. In practice though, simultaneous retrieval is sensitive to errors in the image disparities due to the strong coupling of motion and height in the image disparity. Pre-launch simulation and post-launch testing both indicate a propagation of errors leading to ± 3 m/s in cloud advection and ± 800 m in cloud-top height. Such retrievals should prove to be of sufficient accuracy to be useful in global descriptions of cloud properties, especially because they are based directly on a stereophotogrammetric approach that, unlike many other cloud-top height retrieval approaches, makes no *a priori* climatological assumptions about atmospheric temperature/height relationships. Over the course of the Terra mission, comparisons will be made between MISR stereo cloud-top heights and split-window CO2 thermal IR heights from the Moderate resolution Image Spectroradiometer (MODIS) (King *et al.*, 1992), which will yield further insights into the accuracy and unique attribute of the stereo approach.

Acknowledgments

The authors gratefully acknowledge the efforts of MISR Science team member J.V. Martonchik and the MISR Science Data System Team: M.D. Apolinski, E.G. Hansen, V.M. Jovanovic, and C.M. Moroney. This work was carried out at the Jet Propulsion Laboratory, California Institute of Technology, under a contract with the National Aeronautics and Space Administration. For further information, see the MISR web site at http://www-misr.jpl.nasa.gov.

References

Diner, D.J., J.C. Beckert, T.H. Reilly, T.P. Ackerman, C.J. Bruegge, J.E. Conel, R. Davies, S.A.W. Gerstl, H.R. Gordon, R.A. Kahn, J.V. Martonchik, J.-P. Muller, R. Myneni, B. Pinty, P.J. Sellers, and M.M. Verstraete, 1998. Multi-angle Imaging SpectroRadiometer (MISR):

Instrument description and experiment overview, *IEEE Transactions on Geoscience and Remote Sensing*, 36(4):1072–1087.

Diner, D.J., R. Davies, T. Várnai, C. Moroney, C. Borel, S.A.W. Gerstl, and D.L. Nelson, 1999a. *Level 2 Top-of-Atmospheric Albedo Algorithm Theoretical Basis*, JPL Internal Document D-13401, Rev. D, Jet Propulsion Laboratory, Pasadena, California, 81 p.

Diner, D.J., R. Davies, L. Di Girolamo, Á. Horváth, C. Moroney, J. Muller, S.R. Paradise, D. Wenkert, and J. Zong, 1999b. *Level 2 Cloud Detection and Classification Algorithm Theoretical Basis*, JPL Internal Document D-11399, Rev. D, Jet Propulsion Laboratory, Pasadena, California, 102 p.

Hasler, A.F., 1981. Stereographic observations from geosynchronous satellite: An important new tool for the atmospheric sciences, *Bulletin, American Meteorological Society*, 62:194–212.

Horváth, Á., and R. Davies, 2000. Feasibility and error analysis of cloud motion and wind extraction from near-simultaneous multiangle MISR measurements, *Journal of Atmospheric and Oceanic Technology*, 18(4):591–608.

———, 2001. Simultaneous retrieval of cloud motion and height from polar-orbiter multiangle measurements, *Geophysical Research Letters*, 28:2915–2918.

Jovanovic, V.M., M.M. Smyth, and J. Zong, 1996. Autonomous and Continuous Georectification of Multi-angle Imaging SpectroRadiometer (MISR) imagery, *ISPRS International Archives of Photogrammetry*, 18(Comm. II):176–181.

Kassander, A.R., Jr., and L.L. Simms, 1957. Cloud photogrammetry with ground-located K-17 aerial cameras, *Journal of Meteorology*, 14:43–49.

Kim, T., 2000. A study on the epipolarity of linear pushbroom images, *Photogrammetric Engineering & Remote Sensing*, 66(8):961–966.

King, M. D., Y. J. Kaufmann, W. P. Menzel, and D. Tanre, 1992. Remote sensing of cloud, aerosol, and water vapour properties from the Moderate Resolution Imaging Spectrometer (MODIS)., *IEEE Transactions on Geoscience and Remote Sensing*, 30:2–27.

Lewicki, S.A., M.M. Smyth, V.M. Jovanovic, and E.G. Hansen, 1994. Simulation of EOS MISR data and geometric processing for the prototyping of the MISR ground data system, IGARSS, 08-12 August, Pasadena, California, 3:1543–1545.

Lorenz, D., 1983. Stereoscopic imaging from polar orbit and synthetic stereo imaging, *Advanced Space Research*, 2:133–136.

———, 1985. On the feasibility of cloud stereoscopy and wind determination with the along-track scanning radiometer, *International Journal of Remote Sensing*, 6(8):1445–1461.

Minzer, R.A., W.E. Shenk, R.D. Teagle, and J. Steranka, 1978. Stereographic cloud heights from imagery of SMS/GOES satellites, *Geophysical Research Letters*, 5(1):21–24.

Prata, A.J., and P.J. Turner, 1997. Cloud-top height determination using ATSR data, *Remote Sensing of Environment*, 59:1–13.

Roach, W.T., 1967. On the nature of the summit areas of severe storms in Oklahoma, *Quarterly Journal of the Royal Meteorological Society*, 93:318.

Snyder, J., 1987. Map Projections - A Working Manual, U.S. Geological Survey Professional Paper 1395, U.S. Government Printing Office, Washington, D.C., 214 p.

(Received 10 May 2000; revised and accepted 26 December 2001)